

# Self-Assembled Arginine-Capped Peptide Bolaamphiphile Nanosheets for Cell Culture and Controlled Wettability Surfaces

Emerson Rodrigo da Silva,<sup>\*,†,‡</sup> Merlin Nathaniel Mark Walter,<sup>§</sup> Mehedi Reza,<sup>||</sup> Valeria Castelletto,<sup>‡</sup> Janne Ruokolainen,<sup>||</sup> Che John Connolly,<sup>§</sup> Wendel Andrade Alves,<sup>†</sup> and Ian William Hamley<sup>\*,‡</sup>

<sup>†</sup>Centro de Ciências Naturais e Humanas, Universidade Federal do ABC, Santo André 09210-580, Brazil

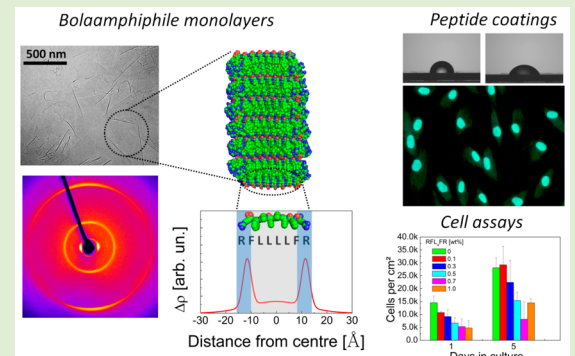
<sup>‡</sup>Department of Chemistry, University of Reading, Whiteknights, Reading RG6 6AD, United Kingdom

<sup>§</sup>Institute of Genetic Medicine, Newcastle University, International Centre for Life, Central Parkway, Newcastle upon Tyne NE1 3BZ, United Kingdom

<sup>||</sup>Department of Applied Physics, Aalto University School of Science, P.O. Box 15100, FI-00076 Aalto, Finland

## Supporting Information

**ABSTRACT:** The spontaneous assembly of a peptide bolaamphiphile in water, namely, RFL<sub>4</sub>FR (R, arginine; F, phenylalanine; L, leucine) is investigated, along with its novel properties in surface modification and usage as substrates for cell culture. RFL<sub>4</sub>FR self-assembles into nanosheets through lateral association of the peptide backbone. The L<sub>4</sub> sequence is located within the core of the nanosheets, whereas the R moieties are exposed to the water at the surface of the nanosheets. Kinetic assays indicate that the self-assembly is driven by a remarkable two-step process, where a nucleation phase is followed by fast growth of nanosheets with an autocatalysis process. The internal structure of the nanosheets is formed from ultrathin bolaamphiphile monolayers with a crystalline orthorhombic symmetry with cross- $\beta$  organization. We show that human corneal stromal fibroblast (hCSF) cells can grow on polystyrene films coated with films dried from RFL<sub>4</sub>FR solutions. For the first time, this type of amphiphilic peptide is used as a substrate to modulate the wettability of solid surfaces for cell culture applications.



## INTRODUCTION

The self-assembly of short peptides into ordered nanostructures is widely used as a tool for the development of new materials in biotechnology and related fields.<sup>1,2</sup> Peptide-based nanomaterials present both an intrinsic biocompatibility and rich structural diversity because their building blocks are amino acids.<sup>3</sup> In particular, peptide amphiphiles (PAs) have been a popular choice to formulate peptide biomaterials because of their ability to self-assemble in aqueous medium and their versatile design, where biofunctionality can be easily introduced through the appropriate linkage of specific amino acid sequences.<sup>2</sup>

During the last 3 decades, the self-assembly of synthetic PAs has been extensively characterized, and their interaction with plasma membranes has been investigated.<sup>4,5</sup> More recently, there has been increasing interest in the development of new peptide materials with bioactive units that are suitable to produce coatings for cell culture<sup>6</sup> and antimicrobial surfaces.<sup>7,8</sup> Bioinspired moieties, derived from functional domains available in naturally occurring proteins, have often been used to design sequences with enhanced cell attachment and proliferation properties.<sup>9,10</sup> The lipopeptide C<sub>16</sub>-KTTKS, incorporating a pentapeptide segment from human collagen type I, has been found to stimulate collagen production in a concentration-

dependent manner in both dermal and corneal fibroblast cultures.<sup>11</sup> Also, peptide films containing the fibronectin epitope RGDS (R, arginine; G, glycine; D, aspartic acid; S, serine) show good adhesion properties and can significantly enhance the proliferation of human cornea stromal fibroblasts (hCSF).<sup>10,12–14</sup> Arginine-rich sequences are often used in the synthesis of PAs with antimicrobial<sup>7</sup> and cell membrane-permeation capabilities.<sup>15</sup> In addition, the extensive presence of arginine residues in cell-penetrating oligopeptides such as the transactivator of transcription of HIV-I and the penetratin sequence derived from *Drosophila* Antennapedia protein also inspires its usage in cell-targetting substrates.<sup>16</sup> The exact mechanism by which arginine-based peptides exhibit higher membrane permeation across the cytoplasmic barrier remains elusive. However, it has been proposed that the positive charge might favor association with anionic species in the cell membrane, whereas the planar Y-shaped geometry and the strong H-bond-donating capabilities of the guanidinium groups

Received: June 19, 2015

Revised: September 3, 2015

Published: September 8, 2015

in the R residue could induce negative curvature, resulting in caveolae and membrane disruption.<sup>15</sup>

The vast majority of reports on self-assembling PAs describe surfactant-like species, with a polar head consisting of a short hydrophilic sequence linked to a longer hydrophobic tail of nonpolar amino acids or lipidated hydrocarbon chains.<sup>17,18</sup> An interesting alternative to this common layout is that within so-called bolaamphiphilic peptides. They consist of hydrophilic peptide groups at both ends of a relatively long hydrophobic hydrocarbon chain or peptide sequence. The double-headed design of bolaamphiphilic peptides increases solubility and makes possible the formation of nanostructures with well-defined external hydrophilic surfaces.<sup>19</sup> In particular, the higher propensity of bolaamphiphilic peptides to self-assemble into flat layers through lateral association of hydrophobic cores<sup>20</sup> makes them good candidates for the formulation of coating substrates.

Although these characteristics make bolaamphiphiles attractive for developing peptide coatings, research on these compounds has been rarely reported in the literature. To the best of our knowledge, there has been no previous work on the self-assembly and cytotoxicity properties of double-headed arginine-based peptides. Here, we present a detailed investigation of the self-assembly and cytotoxicity of the linear octamer RFL<sub>4</sub>FR (R, arginine; F, phenylalanine; L, leucine). The core of RFL<sub>4</sub>FR consists of the strongly hydrophobic tetraleucine segment containing aliphatic side chains.<sup>18</sup> The central spacer is flanked on either side by F residues, which favors self-assembly through  $\pi-\pi$  interactions between neighboring chains, as recently observed.<sup>21,22</sup> The polar ends of the peptide sequence are made from cationic arginine groups with cell attachment properties, exploited in the creation of substrates for cell culture using RFL<sub>4</sub>FR. In the following sections, we probe the structure of RFL<sub>4</sub>FR using X-ray diffraction (XRD), small-angle neutron and X-ray scattering (SANS and SAXS), circular dichroism (CD) spectroscopy, and cryogenic transmission electron microscopy (cryo-TEM). Kinetic data following the time evolution of secondary structure through CD provides unique insights on the self-assembly pathway. The remarkable ability of this peptide to modulate wettability properties on solid substrates is investigated by contact angle measurements and AFM imaging. The cytotoxicity of RFL<sub>4</sub>FR coatings is investigated through live/dead fluorescence assays conducted using fibroblast cells *in vitro*.

Results from a range of techniques show that, above a critical aggregation concentration, RFL<sub>4</sub>FR aggregates into ultrathin flat sheets based on  $\beta$ -sheet assemblies. Notably, kinetic measurements of secondary structure suggest that self-assembly is triggered by a nucleation process. We finally show, for the first time, that bolaamphiphilic peptide nanotapes can be used to produce arginine-rich coatings for cell culture by drying solutions containing up to ~0.1 wt % RFL<sub>4</sub>FR.

## METHODS

**Peptide Synthesis and Samples Preparation.** Peptides were custom-synthesized by CS Bio (Menlo Park, CA) using TFA as a counterion (catalog no. CS12075, batch N013). Purity was assessed by HPLC to be 97.53%. The mass was determined by electrospray mass spectrometry to be 1076.86 Da (expected: 1076.36). The dry powder was refrigerated at -20 °C, and samples were prepared just by dissolving weighed amounts into ultrapure water from a Barnsted Nanopure system (or D<sub>2</sub>O from Sigma-Aldrich). After mixing, samples were submitted to ultrasonication for ~30 min at 60 °C to ensure solubilization. Peptides were considered to be completely dissolved when solutions became transparent.

**Fluorescence Assays.** Samples containing between  $\sim 10^{-5}$  and  $\sim 1$  wt % peptide were dissolved into solutions containing  $1 \times 10^{-5}$  wt % pyrene. Samples were incubated overnight at room temperature (RT, 20 °C) prior to fluorescence assays. Data were recorded using a Cary Varian Ellipse spectrometer, with excitation wavelength  $\lambda_{\text{exc}} = 338$  nm and slits at  $5 \times 5$  nm. Fluorescence intensities at 375 nm were plotted as a function of log[peptide concentration], and the critical aggregation concentration (cac) was estimated from the crossover between linear fits corresponding to different emission regimes.

**Fourier Transform Infrared (FTIR).** Spectra were obtained on a Nicolet Nexus spectrometer. Droplets of peptide dissolved in D<sub>2</sub>O were sandwiched between CaF<sub>2</sub> windows with mica spacers of 12  $\mu$ m. One-hundred and twenty eight accumulations were obtained using a resolution of 4 cm<sup>-1</sup>. The data were corrected by subtraction of the D<sub>2</sub>O spectra.

**Synchrotron Radiation Circular Dichroism (SRCD).** Data were obtained on module B of the B23 beamline at Diamond Light Source (Didcot, UK). Hellma cuvettes with path lengths of 0.01, 0.2, or 1 mm, depending on concentration, were used to optimize the signal-to-noise ratio, with the absorbance values  $A < 2$ . The ring current was 230 mA, and the beamline parameters were as follows: 1 mm slits, 1 nm per step, 1 s per step, and 1 nm bandwidth. Data were averaged over 4 accumulations, and background was subtracted. Raw data were converted into mean residue ellipticity units to allow comparison between different concentrations and path lengths. Kinetic data were obtained using a sealed cuvette to avoid evaporation. The temperature was kept at 20 °C, spectra were obtained every 10 min, and the data collection started only after ultrasonication and thermal equilibration.

**Cryo-Transmission Electron Microscopy (Cryo-TEM).** Imaging was performed as described elsewhere.<sup>10</sup> The instrument was a cryo-electron microscope, JEOL JEM-3200FSC, with an acceleration voltage of 300 kV. The device was used in bright-field mode with a slit width of 20 eV, and images were recorded with a Gatan Ultrascan 4000 CCD camera. Aliquots of 3  $\mu$ L of solution were cast on copper grids, blotted once for 1 s, and then vitrified (in a FEI Vitrobot device) in a 1:1 mixture of liquid ethane and propane at -180 °C. Grids with vitrified samples were maintained in liquid nitrogen and then cryotransferred into the microscope.

**X-ray diffraction (XRD).** Patterns from oriented samples were obtained from dried stalks. Droplets of a 5 wt % peptide solution were suspended between the ends of wax-coated capillaries and allowed to dry at room temperature. Stalks were vertically positioned onto a RAXIS IV++X-ray diffractometer (Rigaku) using a rotating anode generator as the X-ray source. Data were registered using a Saturn 992 CCD camera at a sample-to-detector distance of 40 mm. Data reduction was performed using Fit2D software (ESRF), and unit cell optimization and simulations were carried out with the program CLEARER.<sup>23</sup>

**Synchrotron Small-Angle X-ray Scattering (SAXS).** Experiments were performed using the bioSAXS set up on beamline BM29 at ESRF (Grenoble, France). Amounts,  $\sim 50 \mu$ L, of peptide solution were injected into a 1 mm quartz capillary and flowed during data acquisition to avoid radiation damage. Typically, 30 frames of 0.2 s each were registered and compared and, if no radiation damage was detected, averaged. Buffer measurements were performed before and after each sample measurement. The X-ray wavelength was  $\lambda = 0.91$  Å, and sample-to-detector distance was 2864 mm. The  $q$  range was in the interval  $0.04 \text{ nm}^{-1} \leq q \leq 4.9 \text{ nm}^{-1}$  (where  $q = 4\pi/\lambda \times \sin \theta$ , with  $2\theta$  being the scattering angle). The detector was a Pilatus 1M. Data were radially averaged and normalized, and background was subtracted using the beamline software. Model fitting was carried out using the Gaussian bilayer form factor available in the software SASfit.

**Small-Angle Neutron Scattering (SANS).** Experiments were carried out on the time-of-flight beamline LOQ at ISIS (Didcot, UK). A 1 wt % peptide solution was prepared using D<sub>2</sub>O as a solvent and transferred into a Hellma banjo cell with a path length of 1 mm. The beam cross-section was 12 mm, the chopper frequency was kept at 25 Hz, and temperature was controlled at 25 °C. A "white" beam, with wavelengths in the range  $2.2 \text{ \AA} \leq \lambda \leq 10 \text{ \AA}$ , illuminated the sample, and scattered neutrons were detected at a distance of about 4 m. Data

was recorded in the interval  $0.01 \text{ \AA}^{-1} \leq q \leq 0.25 \text{ \AA}^{-1}$ . SANS data have been fitted using the step-model presented in the *Supporting Information*, which has been implemented in the *curve fitting toolbox* available in MATLAB. The intermediate angle region was probed on the NIMROD beamline at ISIS. A 1 wt % RFL<sub>4</sub>FR solution prepared into D<sub>2</sub>O was loaded into a silica Hellma cell of  $30 \times 30 \times 1 \text{ mm}^3$  and illuminated with a white beam ( $0.5 \text{ \AA} \leq \lambda \leq 12 \text{ \AA}$ ), with a square cross-section of side 30 mm and incident flight path of 20 m.

**Contact Angle.** Measurements were performed using a GBX-Digidrop instrument. Five microliter water droplets were deposited onto peptide-coated surfaces. Photographs shown in Figures 6A and S2 were taken immediately after casting, and images shown in Figure 7G were obtained  $\sim 10$  min after water deposition. Room temperature was controlled at  $22.5 \pm 1.0 \text{ }^\circ\text{C}$ , and relative humidity was 60%. Angle measurements were obtained using ImageJ software.

**AFM Imaging.** Atomic force microscopy (AFM) assays were carried out at the Brazilian Nanotechnology National Laboratory (Campinas, SP). A Digital Instruments Nanoscope III instrument was operated in tapping mode. Samples were prepared to reproduce the same conditions used in contact angle measurements. Images were obtained by scanning  $512 \times 512$  pixels covering surfaces between 3 and  $10 \mu\text{m}^2$ . Image treatment and roughness measurements were performed with the *Gwyddion* package.

**Cell Assays.** Viability and proliferation assays were performed using human corneal stromal fibroblasts (hCSFs). These cells were isolated from postmortem human corneal rings, following epithelial cell depletion. The tissue was finely minced prior to digestion in 2 mg/mL collagenase type-I (Invitrogen, USA) in Dulbecco's modified Eagle's medium (DMEM) supplemented 5% fetal bovine serum (FBS) for 5 h under gentle agitation at  $37 \text{ }^\circ\text{C}/5\% \text{ CO}_2$ . Isolated cells were plated onto standard culture plates (Corning, USA) and maintained in DMEM/F12 media (Invitrogen) supplemented with 5% FBS, 1 mM ascorbic acid, and 1% penicillin/streptomycin.<sup>6,12</sup> Aqueous RFL<sub>4</sub>FR solutions ranging from 0.1 to 1 wt % peptide were prepared and incubated overnight to ensure the formation of self-assemblies. Peptide films were produced by dropping 50  $\mu\text{L}$  from solutions onto 96-well polystyrene culture plates (Corning, USA) and left to dry overnight at room temperature. Cells were seeded onto the peptide films at approximately  $1 \times 10^4$  cells per  $\text{cm}^2$  and incubated in DMEM/F12 under sterile conditions at  $37 \text{ }^\circ\text{C}/5\% \text{ CO}_2$ . Fluorescence imaging was performed after 24 h and on day 5 after seeding. Prior to fluorescence assays, cell culture media was removed, wells were gently rinsed three times with sterile phosphate buffered saline (PBS), and a live/dead double staining assay (Calbiochem) was performed according to the manufacturer's instructions. Briefly, this assay consists of two fluorescent dyes: the membrane-permeable Cyto-Dye (fluorescence in green) and membrane-impermeable propidium iodide (fluorescence in red). Cells were incubated for 15 min with both dyes before again being rinsed three times with PBS. Fluorescence images were registered using an AxioVert 200 (Zeiss) microscope. Green and red fluorescence images were obtained using separate filters and superposed with ImageJ. In the superposed image, live cells display green cytoplasmic staining only, whereas dead cells exhibit a red nuclear stain. Live and dead cells were manually counted. Averages and standard deviations were obtained over triplicates.

## RESULTS

The critical aggregation concentration (cac) of the RFL<sub>4</sub>FR bolaamphiphile was assessed using a pyrene fluorescence assay. Peptide solutions containing from  $3 \times 10^{-5}$  to 1 wt % RFL<sub>4</sub>FR were prepared using a  $1 \times 10^{-5}$  wt % pyrene solution as the solvent. The fluorescence emission of the solutions ( $\lambda_{\text{ex}} = 338 \text{ nm}$ ) was monitored in the interval 350–450 nm. In Figure 1A, the emission intensity at 373 nm is shown as a function of peptide concentration, revealing a sharp transition around a cac  $\sim 0.085 \text{ wt \%}$ . The discontinuity in the concentration dependence of the fluorescence intensity indicates the trapping of pyrene molecules within the hydrophobic core of peptide

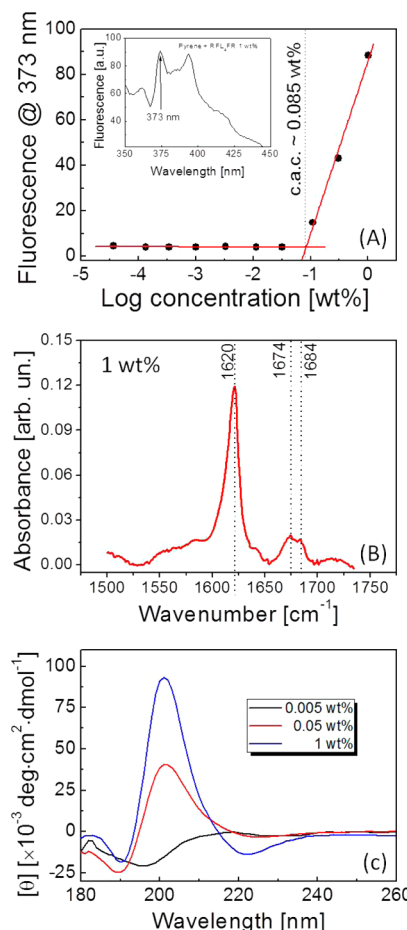


**Figure 1.** (A) Fluorescence data from peptide solutions containing  $1.3 \times 10^{-3}$  wt % pyrene ( $\lambda_{\text{ex}} = 338 \text{ nm}$ ). (B) FTIR spectrum showing the amide I and II regions measured for a 1 wt % RFL<sub>4</sub>FR solution. (C) CD spectra from solutions below and above the cac.

aggregates formed above the critical concentration.<sup>24,25</sup> The cac found for RFL<sub>4</sub>FR is relatively low compared to the values obtained for single-headed arginine-rich amphiphiles investigated recently.<sup>10,12</sup> For instance, peptides A<sub>6</sub>RGD and A<sub>6</sub>R, whose hydrophobic tails are composed of alanine residues, show aggregation concentrations around one order of magnitude higher than that reported in Figure 1.<sup>10,26</sup> This finding is especially interesting considering that the presence of a second polar head is expected to increase solubility of the sequence,<sup>19,20</sup> and it points to the unique composition of the bolaamphiphile investigated here. Previous studies have noted the lowering of critical concentrations in bolaamphiphile self-assemblies due to the formation of H-bond networks induced by amide linkages along peptide backbones.<sup>27–29</sup> In the case of RFL<sub>4</sub>FR, not only amide groups but also guanidinium moieties within arginine residues are likely a source of H-bond donors that contribute toward stabilizing self-assemblies at lower concentrations. A<sub>6</sub>RGD peptides also exhibit backbones rich in amide linkages, but the lack of a second arginine group decreases its abilities to form H-bond networks and could play a role in its higher cac. In addition to H-bonding between adjacent strands, the entropy gain arising from the hydrophobic effect is also an indispensable driving force of self-assembly at low concentrations. In fact, H-bonding alone is not enough to stabilize well-ordered nanosized structures in aqueous medium due to compensation of enthalpy gain by entropy loss upon H-

bond formation.<sup>27,30,31</sup> Regarding RFL<sub>4</sub>FR, we presume that the tetraleucine segment flanked by phenylalanine moieties boosts the amphipathic nature of the bolaamphiphile. Indeed, the RFL<sub>4</sub>FR bolaamphiphile exhibits an average Kyte–Doolittle<sup>32</sup> hydrophathy  $\sim 1.5$ , whereas, for A<sub>6</sub>RGD and A<sub>6</sub>R sequences, these averages are  $\sim 0.3$  and  $\sim 0.9$ , respectively.

The secondary structure of the peptide in solution has been analyzed using FTIR and CD. The amide region of the FTIR spectrum obtained for a 1 wt % solution shows a very sharp peak at 1620 cm<sup>-1</sup> (Figure 1B), assigned to a  $\beta$ -sheet conformation.<sup>33</sup> Figure 1B also shows two bands at 1674 and 1684 cm<sup>-1</sup> attributed to TFA counterions bound to R residues<sup>34</sup> and to the antiparallel  $\beta$ -sheet conformation, respectively.<sup>33</sup> In Figure 1C, CD data from three mixtures below and above the cac show a close relationship between peptide conformation and concentration. The spectrum for the sample prepared at 0.005 wt % RFL<sub>4</sub>FR exhibits a minimum around 192 nm and a shallow positive maximum at  $\sim 218$  nm, associated with mixed transitions arising from peptide backbone and phenylalanine residues in an unordered conformation.<sup>35</sup> At a higher concentration, 0.05 wt % RFL<sub>4</sub>FR, the spectrum reveals some features typically found in  $\beta$ -sheet structures. In this case, a small negative peak is noticed at  $\sim 190$  nm and a strong maximum is found at  $\sim 200$  nm, along with a broad minimum near 220 nm. These features suggest the formation of  $\beta$ -sheet structures in the vicinity of the cac. The  $\beta$ -sheet characteristics are even more evident at 1 wt % peptide, with an intense 200 nm maximum appearing accompanied by a shallow (red-shifted) minimum at  $\sim 220$  nm.

CD is a valuable tool to investigate the time evolution of peptide aggregation and protein folding in solution.<sup>36,37</sup> Here, we followed the kinetics of evolution of the secondary structure of RFL<sub>4</sub>FR to provide insight into the self-assembly pathway of this bolaamphiphile. Figure 2 shows CD data measured for a

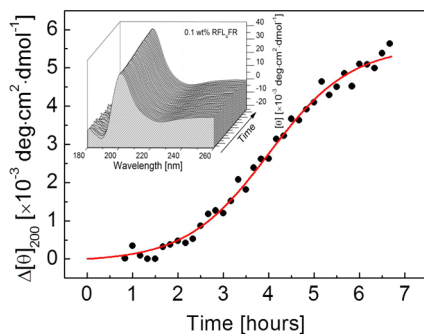


**Figure 2.** Molar ellipticity at  $\lambda = 200$  nm as a function of elapsed time after dissolution (0.1 wt % RFL<sub>4</sub>FR solution). Data have been normalized to an initial minimum of zero and fitted using eq 1, providing  $k_1 = 1.32 \pm 0.04 \times 10^{-2} \text{ h}^{-1}$  and  $k_2 = 1.96 \pm 0.35 \times 10^{-1} \text{ mM}^{-1} \cdot \text{h}^{-1}$ . Inset: CD time series showing  $\beta$ -sheet features.

0.1 wt % solution recorded for times between  $\sim 45$  min and 7 h after the start of mixing the peptide in water. The need for heating and sonication to ensure complete dissolution of the peptide in water, followed by cooling to room temperature, prevented data collection for the first 45 min after putting the peptide in contact with water. Characteristic  $\beta$ -sheet features are observed at the early stages of aggregation, and the spectra are dominated by the remarkable positive maximum at  $\sim 200$  nm (Figure 2, inset). These findings suggest rapid formation of  $\beta$ -sheet cores already during the dissolution process, which

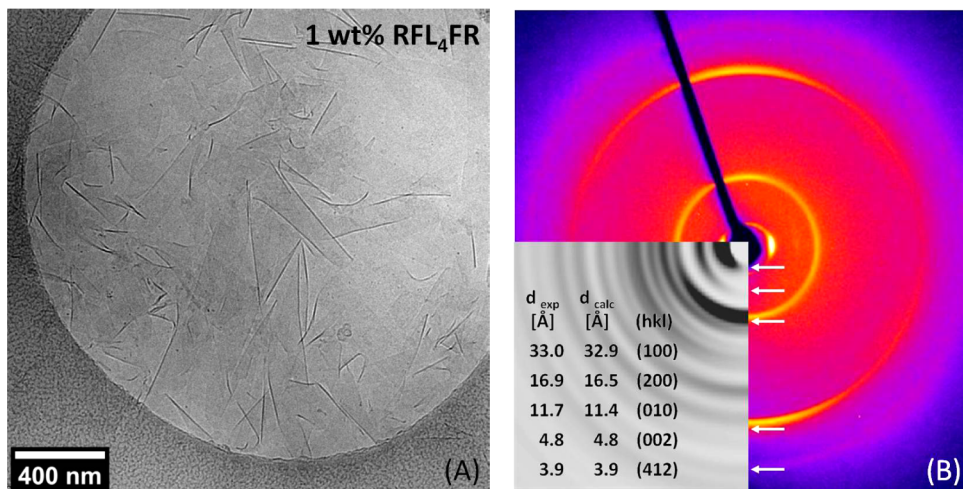
presumably results from the strong amphiphilicity of the RFL<sub>4</sub>FR sequence. In the following, we assume that the ellipticity at  $\sim 200$  nm is proportional to the number of  $\beta$ -sheets in solution. It should be mentioned that other conformational changes not necessarily related to the self-assembly could play a role in the CD spectra. However, using methods described previously,<sup>38</sup> useful kinetic information can be obtained from the procedure described below.

Figure 2 indicates that the time evolution of ellipticity at 200 nm follows a sigmoidal profile similar to typical signatures found in a large variety of protein aggregation processes.<sup>39</sup> To describe this behavior, we have used the two-step model proposed by Finke and Watzky (F–W).<sup>38,40,41</sup> The F–W model describes two self-assembly reactions,  $A \rightarrow B$  and  $A + B \rightarrow 2B$ , where A represents the monomeric form of the protein and B is the monomer incorporated into an aggregate.<sup>40,42</sup> It should be noted that these reactions are composed of a multitude of elementary steps (monomers  $\rightarrow$  dimers  $\rightarrow$  trimers  $\rightarrow \dots$ ) and that their corresponding constant rates,  $k_1$  and  $k_2$ , embody average values for all underlying steps.<sup>38</sup> The model comprises a slow nucleation phase, where monomers are converted into aggregated nucleation centers, and a fast growth with primary species absorbing onto the nucleation centers and forming well-developed aggregates. Although the two-step model does not account for underlying molecular mechanisms present in aggregation, it has been successful at providing average rates, which allow comparison between data sets from different proteins.<sup>38,41</sup> Also, it should be noted that nanosheets are both a catalyst and a product; thus, the second part of the reaction represents an autocatalysis process.<sup>41</sup>

Mathematically, the model is expressed in its integrated form by the simple three-parameter equation<sup>38,41</sup>

$$[B]_t = [A]_0 - \frac{\frac{k_1}{k_2} + [A]_0}{1 + \frac{k_1}{k_2[A]_0} \exp(k_1 + k_2[A]_0)t} \quad (1)$$

$[B]_t$  and  $[A]_0$  are proportional to the concentration of aggregates at time  $t$  and the initial concentration of protein, respectively.<sup>41</sup> Parameters  $k_1$  and  $k_2$  are average rate constants related to characteristic times of nucleation and autocatalytic growth. Equation 1 has been extensively used to fit kinetic data sets from a number of proteins undergoing folding and peptides aggregating into amyloid fibrils, as investigated through a wide variety of physical methods, including CD.<sup>39,43,44</sup> In addition, it is one of the simplest nonempirical functions providing average kinetic constants to describe the macroscopic behavior of aggregation.<sup>41</sup> We have normalized our data to an initial minimum of zero and used eq 1 to fit the temporal variation of ellipticity. As indicated by the red line in Figure 2, the fit exhibits very good agreement with experimental points, although only three parameters are left free in the model. Parameter  $[A]_0$  has been found to be at  $5.56 [\times 10^{-3} \text{ deg} \cdot \text{cm}^2 \cdot \text{dmol}^{-1}]$ , and here it is associated with the ellipticity (at 200 nm) induced by the self-assembly. The resulting rate constants  $k_1 = 1.32 \pm 0.04 \times 10^{-2} \text{ h}^{-1}$  and  $k_2 = 1.96 \pm 0.35 \times 10^{-1} \text{ mM}^{-1} \cdot \text{h}^{-1}$  are around one order of magnitude lower than those found in other protein analogs and show that the self-assembly of this short bolaamphiphilic peptide is relatively fast compared, for example, to that of the amyloid fibril formation of A $\beta$  segments investigated under similar conditions.<sup>36–38</sup> In addition, this relatively quick self-assembly process at a



**Figure 3.** (A) Cryo-TEM image from a vitrified 1 wt % solution showing extensive formation of peptide nanosheets. (B) XRD pattern from a dried stalk containing partially aligned RFL<sub>4</sub>FR sheets. White arrows highlight diffraction rings also identified in the experimental pattern. Inset: Theoretical pattern simulated using an orthorhombic unit cell with the following parameters:  $a = 32.9 \text{ \AA}$ ,  $b = 11.4 \text{ \AA}$ , and  $c = 9.6 \text{ \AA}$ .

concentration close to the cac is consistent with the strong amphiphilicity of RFL<sub>4</sub>FR.

To investigate the morphology of the structures resulting from the self-assembly, cryo-TEM imaging has been performed on vitrified specimens. Figure 3A shows a representative micrograph from a 1 wt % RFL<sub>4</sub>FR solution, revealing the formation of extensive peptide nanosheets. Additional images can be found in Supporting Information, Figure S1. The formed membranes are apparently highly homogeneous in thickness and exhibit defect-free interfaces with large surface areas. Also, the micrographs show that the sheets are highly flexible, since partially folded edges are clearly identified. These characteristics suggest an interesting potential for using these peptide sheets as arginine-rich films for coating substrates and subsequent exploration in cell-related applications, as discussed below.

The molecular packing within nanosheets has been probed through XRD experiments performed on dried stalks. In Figure 3B, a partially oriented pattern shows intense diffraction rings, indicating a high degree of ordering within the fibrils. Diffraction data from oriented samples systematically reveal sharp meridional reflections at  $d = 4.8 \text{ \AA}$ . This repeat distance has been widely ascribed to separation between hydrogen-bonded  $\beta$ -strands organized into  $\beta$ -sheets either in peptides or protein aggregates.<sup>45,46</sup> In the case of the RFL<sub>4</sub>FR assemblies, we find ordering of anti-parallel-aligned strands with periodicity  $d = 4.8 \text{ \AA}$  and held together by H-bonds between NH and CO groups along the backbones.<sup>2</sup> This information also agrees with FTIR and CD data shown in Figure 1. In addition to the strong meridional reflection, the XRD pattern also contains peaks corresponding to  $d = 11.7 \text{ \AA}$ , which are also found by neutron scattering for samples in solution, as discussed below (Figure 5, inset). This periodicity arises from the intersheet spacing between laterally stacked  $\beta$ -sheets, likely stabilized through H-bonds between guanidinium groups at polar termini or through  $\pi$ -stacking of aromatic rings in phenylalanine's side chain. From the results derived above, we conclude that self-assemblies are formed by galleries of strands separated by steps of  $4.8 \text{ \AA}$  along the parallel direction and associated into indefinitely long  $\beta$ -sheets laterally spaced by distances of about  $11.7 \text{ \AA}$ . In the third direction, i.e., perpendicular to the plane of nanosheets, the size is determined by the molecular length of RFL<sub>4</sub>FR. Closer to the

beam stop, two very strong peaks are found that correspond to spacings  $d = 33.0 \text{ \AA}$ , consistent with the length of a octapeptide chain ( $8 \times 3.5 \text{ \AA} = 28 \text{ \AA}$ ) plus TFA counterions adsorbed onto arginine groups.<sup>47</sup> These reflections appear along the equator of the figure, oriented perpendicularly to the diffraction from the  $\beta$ -strand spacing. This configuration confirms that the sheets are organized into a cross- $\beta$  structure<sup>48</sup> self-assembled through lateral association between RFL<sub>4</sub>FR chains.<sup>46</sup> In addition to the strong diffraction peaks mentioned above, other weaker spots are observed at  $d = 16.9$  and  $3.9 \text{ \AA}$ . To index this set of Bragg reflections, we have used the unit cell optimization module available in the program CLEARER.<sup>23</sup> Our data have been indexed according to an orthorhombic unit cell with lattice parameters  $a = 32.9 \text{ \AA}$ ,  $b = 11.4 \text{ \AA}$ , and  $c = 9.6 \text{ \AA}$ . To provide a comparison between calculated and experimental data, we have simulated the theoretical diffraction patterns using the parameters from the indexed unit cell. The result is exhibited in the inset of Figure 3B along with the corresponding Miller indices. The simulated pattern accurately describes the major features of the experimental diffractogram, in particular the positions of the Bragg rings are predicted with good precision (see table in Figure 3B, inset). The simulated pattern also exhibits other reflections that are not observed experimentally. The reason for this is related to limitations of the simulation model, which reproduces neither the exact arrangement of side chains nor the crystallite packing.<sup>46</sup>

*In situ* investigations have been performed using synchrotron small-angle X-ray scattering (SAXS) and small-angle neutron scattering (SANS). In Figure 4A, SAXS curves obtained for solutions between 0.1 and 1 wt % RFL<sub>4</sub>FR are exhibited. Across the concentration range, the SAXS profiles are characterized by an intensity decay proportional to  $q^{-2}$  at very low scattering angles, consistent with flat structures<sup>49</sup> and thus in agreement with the morphology revealed by cryo-TEM. Therefore, peptide sheets similar to those observed in Figure 3A are likely present also at lower concentrations. To extract quantitative information, the data was fitted using the bilayer form factor detailed in the Supporting Information, eq S2, and included in the SASFit program. The resulting fits (red lines in Figure 4) show good agreement with the experimental data. The obtained parameters reveal effective membrane thicknesses ranging from 25 to  $29.4 \text{ \AA}$  (see Table S1, Supporting Information), indicating

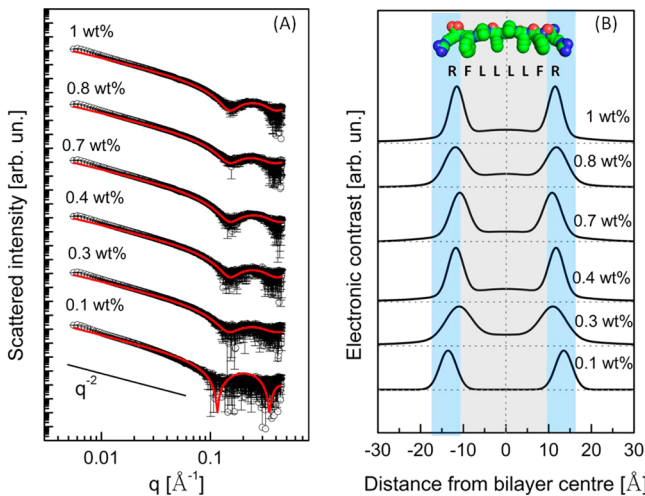


**Figure 4.** (A) SAXS data from peptide solutions at the indicated concentrations. Red lines: model fitting according to a bilayer form factor. (B) Electron density profiles for peptide nanosheets obtained from data fitted in (A). The gray patterned areas indicate the region corresponding to the hydrophobic core composed of a tetraleucine segment flanked by two phenylalanine residues, whereas the regions in blue indicate the rough limits of the polar heads.

that the peptide sheets are made up of bolaamphiphilic monolayers since this thickness is close to the estimated octamer length. It should be noted that, here, the longitudinal size of the peptides appears to be lower than that one revealed by XRD assays because TFA counterions are released from peptide interfaces in solution.

The fitting procedure provides information in addition to layer thickness. Direct-space reconstructions of electron density profiles also have been retrieved by substituting the fitted parameters into eq S4, *Supporting Information*. In Figure 4B, it can be seen that the electron density profiles are dominated by two positive Gaussians, associated with the arginine groups at both termini of the bolaamphiphilic sequence. Interestingly, the central hydrophobic portion is also represented by positive (or neutral) electron density. The electron density for the nonpolar segments is different from profiles observed for other surfactant bilayers, which typically exhibit lower electron densities compared to those of solvent.<sup>50,51</sup> The reason for this unusual behavior is presumably related to the chemical structure of the hydrophobic core in RFL<sub>4</sub>FR, which is made up of amino acid moieties rather than just alkyl chains, as is the case for conventional surfactants and lipids. The extensive presence of side chains and O and N atoms along the backbone leads to higher electron densities in comparison with those of hydrocarbon tails found in lipidated surfactants. In addition, as revealed by XRD experiments, RFL<sub>4</sub>FR chains are organized into a partially crystalline structure; thus, the molecules are closely packed into organized structures.

Neutron scattering provides independent information on the structure of peptide nanosheets since the contrast is related to scattering length densities (SLD) of nuclei in the sample. In Figure 5, SANS data from a 1 wt % RFL<sub>4</sub>FR sample show the same  $q^{-2}$  descent found in the SAXS curves (Figure 4). Due to  $q$ -range constraints and the lower resolution of the SANS measurements, we have implemented the step-model proposed by Nallet et al.<sup>52</sup> and expressed in eq S5 in MatLab to describe the data with a minimal number of parameters. The fit exhibits excellent agreement with the experimental data, highlighting

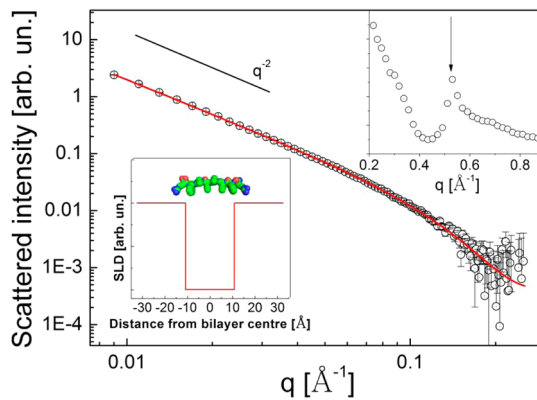


**Figure 5.** SANS data from a 1 wt % RFL<sub>4</sub>FR formulation dissolved in D<sub>2</sub>O. The red line is the best fit according to eq S5 (*Supporting Information*). Insets: (below) Direct-space step-model showing the cross-sectional SLD; (top) scattering data from wide-angle region revealing a Bragg peak (black arrow) associated with a periodicity  $d = 11.9 \text{ \AA}$ .

the robustness of the procedure. The fitted value  $\delta = 21.7 \pm 3.0 \text{ \AA}$  for the thickness of the hydrophobic core is compatible with the membrane thickness revealed by SAXS, within uncertainties. The cross-section SLD profile has been obtained from eq S6 and is reproduced in Figure 5 (inset). Features arising from the structure factor of peptide chains organized within nanosheets appear in the wide-angle region. In Figure 5, inset, we observe a remarkable Bragg peak at  $q = 0.53 \text{ \AA}^{-1}$ , arising from a repeat distance  $d = 11.9 \text{ \AA}$ . This periodicity is consistent with the separation between  $\beta$ -sheets found in XRD assays, thus showing that the  $\beta$ -sheet stacking within the supramolecular structure is also present in solution and is not merely a consequence of drying during the production of stalks for XRD assays.

The solutions studied above have been used to modify solid surfaces and modulate their wettability properties. Samples have been prepared just by casting drops from RFL<sub>4</sub>FR solutions onto the substrates and left to dry overnight. These modified surfaces have been examined through optical microscopy, and the resulting films have been found to be very stable, remaining adsorbed onto the substrates after several weeks or upon mechanical stressing induced by gentle twisting of the surfaces. Contact angle measurements from films obtained from a 0.3 wt % solution are shown in Figure 6A, corresponding to substrates with different degrees of hydrophobicity, a highly wettable (freshly cleaved mica) and quasi-hydrophobic surface (polystyrene, PS). Although the technique is not able to provide a detailed picture of peptide organization on the surfaces, it is very useful for obtaining insights into the average properties.<sup>53</sup> On mica, the contact angle increases from  $0^\circ$  to  $72^\circ$ , showing a dramatic growth of hydrophobicity upon peptide modification. On the other hand, a significant decrease is noticed on PS, from  $86^\circ$  to  $58^\circ$ . On glass surfaces, which exhibit intermediate hydrophilicity, we observed the lowest change from  $38^\circ$  to  $45^\circ$  (*Supporting Information*, Figure S2).

To get deeper insights into the nature of surface modification by peptides, we have performed detailed AFM measurements. Figure 6B shows topology images of samples on mica and PS substrates. AFM data reveal that peptide deposition produces remarkable morphological changes and that coatings with thicknesses of a few hundred nanometers appear to be physically adsorbed on both substrates. Moreover, coatings

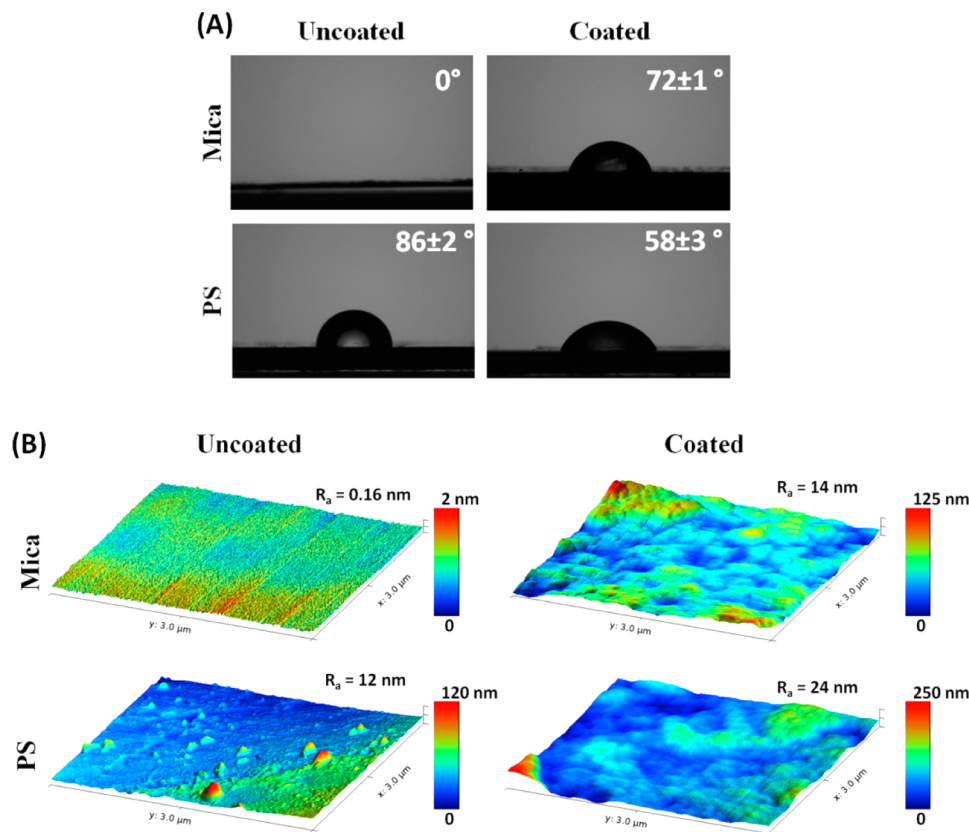


**Figure 6.** (A) Water contact angles from mica and polystyrene substrates modified with RFL<sub>4</sub>FR films. (B) AFM images showing finer topological details and revealing nanoscale roughness of the surfaces ( $3 \times 3 \mu\text{m}^2$ ).

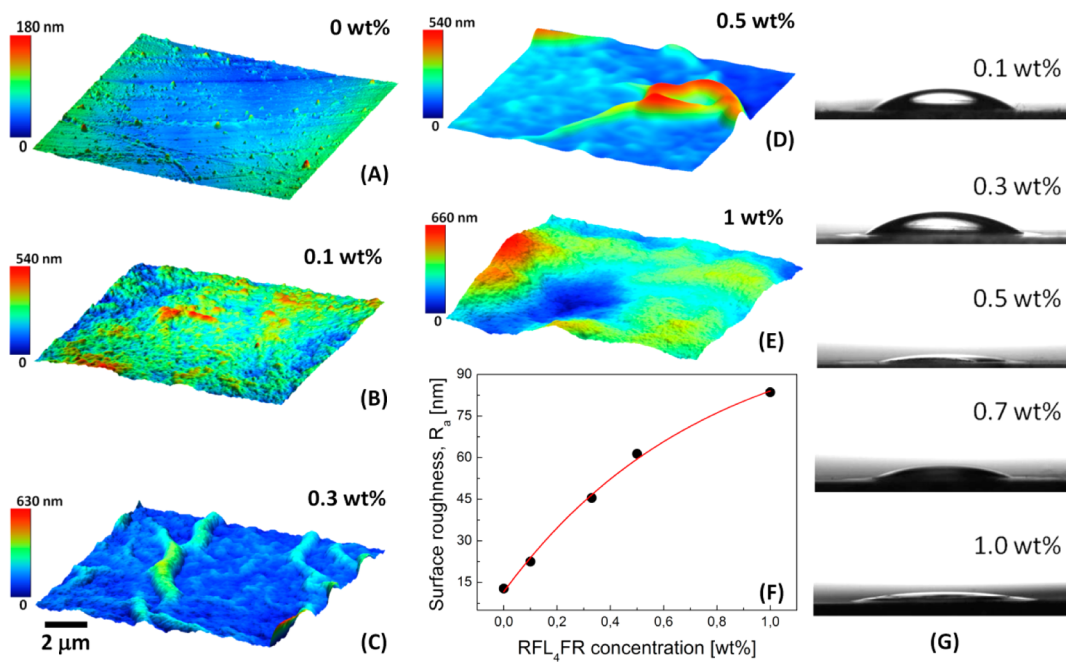


**Figure 7.** (A–E) AFM images showing the topology of RFL<sub>4</sub>FR coatings deposited onto polystyrene surfaces ( $10 \times 10 \mu\text{m}^2$ ). Films were dried from solutions at concentrations indicated. (F) Surface roughness,  $R_a$ , plotted as a function of peptide concentration. Red line: a guide for the eye showing the exponential increase of  $R_a$  with increasing concentration. (G) Water droplets onto coated PS surfaces photographed 10 min after casting.

are homogeneously distributed across the surfaces, and corrugations are restricted to the nanometer scale, indicating the smoothness of peptide coverage. To quantify surface roughness and provide an index for comparison between

different films, we calculated the roughness parameter  $R_a$ , which is defined as the average of absolute vertical deviations from the mean plane (see [Supporting Information](#) for further details). These measurements reveal that roughness is systematically

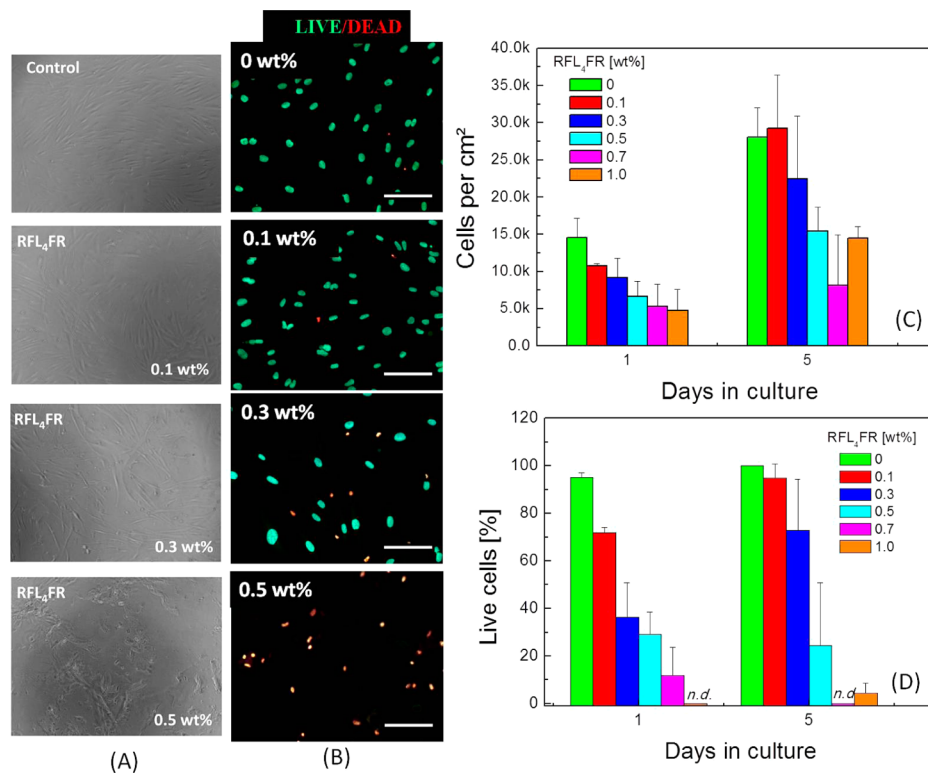


**Figure 8.** Viability assays performed on hCSFs deposited onto peptide films obtained from peptide films dried from solutions at the indicated concentrations. (A) Phase-contrast images registered on day 5. (B) Representative fluorescence images observed on day 5. Live cells appear in green, whereas dead ones exhibit red stained nuclei. (C) Average number of cells per area (mean  $\pm$  SD). (D) Percentage of live cells. (Scale bars: 100  $\mu$ m; n.d., not determined due to absence of cells.)

higher on peptide coatings when compared to that of bare substrates, in agreement with the formation of thicker coatings. Accordingly, freshly cleaved mica exhibits a low roughness parameter  $R_a = 0.16$  nm, whereas peptide films on this same substrate show  $R_a = 14$  nm. On bare and peptide-coated PS, respectively, these values are found to be  $R_a = 12$  and 24 nm. In addition to modulation of roughness induced by peptides, analysis of the roughness parameter reveals interesting insights into the influence of substrate composition on wettability. When we compare roughness and contact angles exhibited in Figure 6, we observe that uncoated PS and peptide-coated mica possess very similar morphologies and exhibit almost the same  $R_a$  values; however, the water hydrophobicity of these materials is rather different, and they possess distinct wettability behaviors. Therefore, in this case, we can infer that the chemical composition of substrates also plays an important role in macroscopic wettability. We hypothesize that the highly hydrophilic and charged nature of the mica surface likely favors adhesion of arginine groups and should assist exposure of nonpolar sites on the top, resulting in stronger hydrophobic behavior. On the other hand, when PS is used as a substrate, the extensive presence of nonpolar clusters could favor polar arginine groups facing upward and increasing polarity at the interface with water.

Previous studies have suggested that both chemical composition and surface morphology contribute toward wettability properties on polymeric substrates used for cell attachment.<sup>54–56</sup> To further characterize the relationship between morphology and wettability, we performed AFM assays on coatings on PS surfaces prepared from solutions in the range 0.1–1 wt %. Topology images associated with these

assays are shown in Figure 7A–E, and they show that morphology is strongly influenced by concentration. Also, although all samples investigated present homogeneous surfaces, data reveal that corrugations become more pronounced when higher amounts of peptide are present. Roughness parameters  $R_a$  have been determined from representative 10  $\times$  10  $\mu$ m<sup>2</sup> surfaces and plotted as a function of peptide concentration in Figure 7F. Interestingly, the roughness increases monotonically upon concentration and exhibits exponential behavior until reaching  $R_a \sim 85$  nm at 1 wt %. Roughness on these surfaces has been correlated to wettability through water contact angle experiments. On films containing higher peptide amounts, droplets appear to be completely spread over the surface after an elapsed time of  $\sim$ 10 min (see Figure 7G), indicating greater wettability possibly due to roughness on these surfaces.

Cell assays have been performed to assess the biocompatibility of RFL<sub>4</sub>FR. In Figure 8A, digital images obtained by phase-contrast microscopy show hCSFs in culture with good adhesion to peptide coatings obtained from solutions containing 0.1 and 0.3 wt % RFL<sub>4</sub>FR. At these concentrations, hCSF cells maintained a typically fibroblastic morphology similar to those observed under standard culture conditions and comparable confluence to controls after 5 days in culture, indicating cell functionality.<sup>10,12,14</sup> Coatings obtained from more concentrated peptide solutions show reduced cellular adhesion and observably rounded, phase-bright cell bodies, indicating nonviable cells. These results were supported by the fluorescent live/dead cell staining (Figure 8B), where only red propidium iodide-stained nuclei (dead cells) were seen for the 0.5 wt % RFL<sub>4</sub>FR solution. The biocompatibility of RFL<sub>4</sub>FR

was quantified by plotting the average cell number density and percentage of viable of attached hCSFs as a function of peptide concentration at 24 h and 5 days postseeding (Figure 8C,D). ANOVA and subsequent *posthoc* testing shows that at day 1 there is a significant difference between films at 0.1 wt % and the control, whereas at day 5, there is no significant difference between these two conditions and the number of cells per  $\text{cm}^2$  is even higher on films at 0.1 wt % (see data for day 5 in Figure 8C). It is clearly shown that both cell number density and percentage viability decline with increasing concentration of peptide in the films. This is most evident during the first day of incubation, indicating poor initial cell attachment at higher concentrations. For instance, on coatings from solutions containing 0.3 wt % RFL<sub>4</sub>FR and above, the number of viable cells is seen to be below 50% of the total number of seeded cells. This increase in cell death is consistent with the higher availability of arginine groups on the substrates, which likely leads to disruption of cell membranes, as reported elsewhere.<sup>15</sup> However, once left to grow for 5 days, cell density increases on coatings up to 0.5 wt %, with no significant differences between the control and 0.1 wt %. The proportion of viable cells also increases accordingly. This suggests that the RFL<sub>4</sub>FR has, indeed, formed a coating even at low concentrations and that cells do not immediately bind to this substrate (as they do to optimized tissue culture plastic; control), but they do require a few days to produce their own supporting extracellular matrix; thus, the coating at low concentrations is not toxic to the fibroblastic cells. However, at higher concentrations, i.e., 0.5% and above, the coating could be considered to be toxic, as a significant difference in cell density was observed even after 5 days. The low attachment of cells on day 1 could be associated with the wettability of peptide-modified surfaces. These findings agree with contact-angle images of RFL<sub>4</sub>FR layers dried from solutions with concentrations above 0.5 wt % (Figure 7G), which show water droplets spread over large areas, suggesting growth of wettability with increasing peptide concentration in the films. In this case, we propose that permeation of water molecules across the coatings is enhanced at higher concentrations and presumably contributes to the detachment of lipid-rich plasma membranes. On the other hand, peptide films prepared from lower concentration solutions show moderate hydrophobicity and seem to be more suitable for cell attachment. This, associated with the lower toxicity of peptides at low concentrations, could enable the formation of the supporting extracellular matrix by the cells.

## CONCLUSIONS

We have examined, for the first time, the self-assembly, secondary structure, wetting properties, and cytocompatibility of an arginine-rich bolaamphiphilic peptide. This peptide has been found to form nanosheets in solution, likely through lateral association between peptide chains, with arginine moieties exposed on both interfaces. The estimated value for critical concentration,  $\text{cac} \sim 0.085$  wt %, is lower than that for many other PAs that have been explored for use in coating materials, and this represents a potential advantage in terms of cytocompatibility. The temporal evolution of self-assembly has been investigated through CD assays, and data have been successfully fitted according to the Finke–Watzy model. This reveals that the self-assembly of RFL<sub>4</sub>FR peptide is driven by a two-step process, where a nucleation phase is followed by fast autocatalytic growth. This is the first time, to our knowledge, that this type of mechanism has been observed for an arginine-

rich oligo-peptide or a bolaamphiphilic peptide. The characteristic rates revealed from these kinetic assays show that time scales for aggregation are on the order of hours, which ensures relatively fast assembly of nanosheets. Secondary structure is dominated by  $\beta$ -sheet conformations, where peptide backbones form paired  $\beta$ -strands with antiparallel orientation. The crystalline structure is characterized by an orthorhombic symmetry with crossed antiparallel strands, at repeat distances of 4.8 Å, forming galleries separated by 11.7 Å running perpendicular to the plane of nanosheets.

Small-angle scattering data shows that the nanosheets are built from bolaamphiphile monolayers. Very good agreement has been found between SAXS and SANS data fitted with a minimum number of free parameters. The electron density profiles of these structures were described by fitting SAXS data to a three Gaussian layer form factor, and they revealed characteristics that are not usual for amphiphilic membranes. Unlike traditional electron density profiles for lipid bilayers or lipidated peptides, the hydrophobic core of RFL<sub>4</sub>FR nanosheets is characterized by a positive contrast, with electron density values above that for the aqueous solvent. This behavior is a direct consequence of the unique design and composition of the peptide bolaamphiphile, where side chains are organized into highly packed structures in the core of the membranes, which produce higher electron densities.

A unique ability to use the bolaamphiphilic peptide to modulate the wettability of different surfaces has been demonstrated by contact angle measurements and deeply characterized through high-resolution AFM analyses. Quantitative determinations on the surface roughness have shown a close relationship between wettability and surface morphology; in addition, chemical interaction between peptide films and the supporting substrate also has been identified. Thus, the macroscopic wettability found in these peptide coatings arises from a combination of physical and chemical characteristics of the assemblies. Our data suggest that adhesion and peptide concentration in the coatings are correlated and that dried films obtained from more concentrated solutions, i.e., above 0.5 wt %, possess poor attachment properties regarding cells. Also, if the peptide content in the film is too high, then cell viability is compromised. These findings are most likely related to the presence of arginine groups in the substrates, since the abundance of cationic groups in the surfaces should lead to higher polarity of the surfaces and thus greater potential to disrupt lipid membranes.<sup>15</sup> No significant differences in cell morphology or viability were observed between the control and films at 0.1 wt % after 5 days in culture, indicating that coatings at this concentration did not introduce detectable cytotoxicity and that cells remain healthy. These data suggest that coatings obtained from 0.1 wt % RFL<sub>4</sub>FR are safe and suitable to interface with living matter.

## ASSOCIATED CONTENT

### Supporting Information

The Supporting Information is available free of charge on the ACS Publications website at DOI: [10.1021/acs.biomac.5b00820](https://doi.org/10.1021/acs.biomac.5b00820).

SAXS and SANS modeling, fitting parameters, and additional contact angle measurements and cryo-TEM images ([PDF](#)).

## AUTHOR INFORMATION

### Corresponding Authors

\*(E.R.d.S.) E-mail: ersilva@ufabc.edu.br; Tel.: +55 11 4996 0035.  
\*(I.W.H.) E-mail: i.w.hamley@reading.ac.uk; Tel.: +44. 0118 378 8453; Fax: +44 0118 378 8505.

### Notes

The authors declare no competing financial interest.

## ACKNOWLEDGMENTS

E.R.d.S. acknowledges FAPESP for a postdoctoral fellowship abroad (Proc. 2014/03514-8 and 2013/12997-0). W.A.A. is grateful to CNPq and FAPESP for grants (400239/2014-0 and 2013/12997-0). I.W.H. is recipient of a Royal Society-Wolfson Research Merit Award, and this work was supported by EPSRC Platform Grant “Nanostructured Polymeric Materials for Healthcare” (EP/L020599/1). We are grateful for the award of synchrotron beamtime at ESRF, proposal MX1666, and Diamond Light Source, proposal SM10083-1. The authors thank Dr. Adam Round (ESRF-BM29) and Dr. Rohanah Hussain (DLS-B23) for help during SAXS and CD experiments. Neutron scattering measurements were performed at ISIS, under proposals RB1510029 and RB1510028. Dr. Stephen King (LOQ beamline) and Dr. Tristan Youngs (NIMROD beamline) are kindly acknowledged for help during neutron experiments. The authors thank Dr. Ricardo Gouveia for instructions and discussions on cell assays. Nick Spencer and Dr. Ashkan Dehsorkhi at UoR are acknowledged for help with XRD measurements. Prof. Hugo Suffredini at UFABC is kindly acknowledged for providing equipment for contact angle measurements. AFM imaging was performed at LCS-LNNano under proposal AFM-19336. Dr. Carlos Costa and Evandro Lanzoni are acknowledged.

## REFERENCES

- (1) de la Rica, R.; Matsui, H. Applications of Peptide and Protein-Based Materials in Bionanotechnology. *Chem. Soc. Rev.* **2010**, *39*, 3499–3509.
- (2) Hamley, I. W. Self-Assembly of Amphiphilic Peptides. *Soft Matter* **2011**, *7*, 4122–4138.
- (3) Reches, M.; Gazit, E. Molecular Self-Assembly of Peptide Nanostructures: Mechanism of Association and Potential Uses. *Curr. Nanosci.* **2006**, *2*, 105–111.
- (4) Binder, H.; Lindblom, G. Charge-Dependent Translocation of the Trojan Peptide Penetratin Across Lipid Membranes. *Biophys. J.* **2003**, *85*, 982–95.
- (5) Pierschbacher, M. D.; Ruoslahti, E. Cell Attachment Activity of Fibronectin can be Duplicated by Small Synthetic Fragments of the Molecule. *Nature* **1984**, *309*, 30–33.
- (6) Gouveia, R. M.; Castelletto, V.; Hamley, I. W.; Connon, C. J. New Self-Assembling Multifunctional Templates for the Biofabrication and Controlled Self-Release of Cultured Tissue. *Tissue Eng., Part A* **2015**, *21*, 1772–1784.
- (7) Zasloff, M. Antimicrobial Peptides of Multicellular Organisms. *Nature* **2002**, *415* (6870), 389–395.
- (8) Hamley, I. W. Lipopeptides: from Self-Assembly to Bioactivity. *Chem. Commun.* **2015**, *51*, 8574–8583.
- (9) Abdul Kafi, M.; El-Said, W. A.; Kim, T. H.; Choi, J. W. Cell Adhesion, Spreading, and Proliferation on Surface Functionalized with RGD Nanopillar Arrays. *Biomaterials* **2012**, *33*, 731–739.
- (10) Castelletto, V.; Gouveia, R. M.; Connon, C. J.; Hamley, I. W.; Seitsonen, J.; Nykanen, A.; Ruokolainen, J. Alanine-Rich Amphiphilic Peptide Containing the RGD Cell Adhesion Motif: a Coating Material for Human Fibroblast Attachment and Culture. *Biomater. Sci.* **2014**, *2*, 362–369.
- (11) Jones, R. R.; Castelletto, V.; Connon, C. J.; Hamley, I. W. Collagen Stimulating Effect of Peptide Amphiphile C16-KTTKS on Human Fibroblasts. *Mol. Pharmaceutics* **2013**, *10*, 1063–1069.
- (12) Gouveia, R. M.; Castelletto, V.; Alcock, S. G.; Hamley, I. W.; Connon, C. J. Bioactive Films Produced from Self-Assembling Peptide Amphiphiles as Versatile Substrates for Tuning Cell Adhesion and Tissue Architecture in Serum-Free Conditions. *J. Mater. Chem. B* **2013**, *1*, 6157–6169.
- (13) Dehsorkhi, A.; Gouveia, R. M.; Smith, A. M.; Hamley, I. W.; Castelletto, V.; Connon, C. J.; Reza, M.; Ruokolainen, J. Self-Assembly of a Dual Functional Bioactive Peptide Amphiphile Incorporating Both Matrix Metalloprotease Substrate and Cell Adhesion Motifs. *Soft Matter* **2015**, *11*, 3115–3124.
- (14) Gouveia, R. M.; Castelletto, V.; Hamley, I. W.; Connon, C. J. New Self-Assembling Multifunctional Templates for the Biofabrication and Controlled Release of Cultured Tissue. *Tissue Eng., Part A* **2015**, *21*, 1772–1784.
- (15) Schmidt, N.; Mishra, A.; Lai, G. H.; Wong, G. C. L. Arginine-Rich Cell-Penetrating Peptides. *FEBS Lett.* **2010**, *584*, 1806–1813.
- (16) Vives, E. Present and Future of Cell-Penetrating Peptide Mediated Delivery Systems: “is the Trojan Horse too Wild to go Only to Troy?”. *J. Controlled Release* **2005**, *109*, 77–85.
- (17) Ulijn, R. V.; Smith, A. M. Designing Peptide Based Nanomaterials. *Chem. Soc. Rev.* **2008**, *37*, 664–675.
- (18) Zhang, S. G. Lipid-Like Self-Assembling Peptides. *Acc. Chem. Res.* **2012**, *45*, 2142–2150.
- (19) Fuhrhop, A. H.; Wang, T. Y. Bolaamphiphiles. *Chem. Rev.* **2004**, *104*, 2901–2937.
- (20) Nuraje, N.; Bai, H. Y.; Su, K. Bolaamphiphilic Molecules: Assembly and Applications. *Prog. Polym. Sci.* **2013**, *38*, 302–343.
- (21) da Silva, E. R.; Alves, W. A.; Castelletto, V.; Reza, M.; Ruokolainen, J.; Hussain, R.; Hamley, I. W. Self-Assembly Pathway of Peptide Nanotubes Formed by a Glutamatic Acid-Based Bolaamphiphile. *Chem. Commun.* **2015**, *51*, 11634–11637.
- (22) Liberato, M. S.; Kogikoski, S.; da Silva, E. R.; Silva, R. H.; Oliveira, V. X.; Scott, L. P.; Ando, R. A.; Coutinho-Neto, M. D.; Alves, W. A. Self-Assembly of Arg-Phe Nanostructures via the Solid-Vapor Phase Method. *J. Phys. Chem. B* **2013**, *117*, 733–740.
- (23) Makin, O. S.; Sikorski, P.; Serpell, L. C. CLEARER: A New Tool for the Analysis of X-ray Fibre Diffraction Patterns and Diffraction Simulation from Atomic Structural Models. *J. Appl. Crystallogr.* **2007**, *40*, 966–972.
- (24) Castelletto, V.; Gouveia, R. M.; Connon, C. J.; Hamley, I. W. New RGD-Peptide Amphiphile Mixtures Containing a Negatively Charged Diluent. *Faraday Discuss.* **2013**, *166*, 381–397.
- (25) Winnik, F. M. Photophysics of Preassociated Pyrenes in Aqueous Polymer-Solutions and in Other Organized Media. *Chem. Rev.* **1993**, *93*, 587–614.
- (26) Hamley, I. W.; Dehsorkhi, A.; Castelletto, V. Self-Assembled Arginine-Coated Peptide Nanosheets in Water. *Chem. Commun.* **2013**, *49*, 1850–1852.
- (27) Shimizu, T. Bottom-Up Synthesis and Morphological Control of High-Axial-Ratio Nanostructures Through Molecular Self-Assembly. *Polym. J.* **2003**, *35*, 1–22.
- (28) Shimizu, T.; Iwaura, R.; Masuda, M.; Hanada, T.; Yase, K. Internucleobase-Interaction-Directed Self-Assembly of Nanofibers from Homo- and Heteroditopic 1, Omega-Nucleobase Bolaamphiphiles. *J. Am. Chem. Soc.* **2001**, *123*, 5947–5955.
- (29) Kogiso, M.; Ohnishi, S.; Yase, K.; Masuda, M.; Shimizu, T. Dicarboxylic Oligopeptide Bolaamphiphiles: Proton-Triggered Self-Assembly of Microtubes with Loose Solid Surfaces. *Langmuir* **1998**, *14*, 4978–4986.
- (30) Ghadiri, M. R.; Granja, J. R.; Milligan, R. A.; McRee, D. E.; Khazanovich, N. Self-Assembling Organic Nanotubes Based on a Cyclic Peptide Architecture. *Nature* **1993**, *366*, 324–327.
- (31) Kimizuka, N.; Kawasaki, T.; Hirata, K.; Kunitake, T. Supramolecular Membranes. Spontaneous Assembly of Aqueous Bilayer Membrane via Formation of Hydrogen Bonded Pairs of

- Melamine and Cyanuric Acid Derivatives. *J. Am. Chem. Soc.* **1998**, *120*, 4094–4104.
- (32) Kyte, J.; Doolittle, R. F. A Simple Method for Displaying the Hydropathic Character of a Protein. *J. Mol. Biol.* **1982**, *157*, 105–132.
- (33) Haris, P. I.; Chapman, D. The Conformational Analysis of Peptides Using Fourier Transform IR Spectroscopy. *Biopolymers* **1995**, *37*, 251–263.
- (34) Eker, F.; Griebenow, K.; Schweitzer-Stenner, R. A Beta(1–28) Fragment of the Amyloid Peptide Predominantly Adopts a Polyproline II Conformation in an Acidic Solution. *Biochemistry* **2004**, *43*, 6893–6898.
- (35) Decandio, C. C.; Silva, E. R.; Hamley, I. W.; Castelletto, V.; Liberato, M. S.; Oliveira, V. X.; Oliveira, C. L. P.; Alves, W. A. Self-Assembly of a Designed Alternating Arginine/Phenylalanine Oligopeptide. *Langmuir* **2015**, *31* (15), 4513–4523.
- (36) Lu, K.; Jacob, J.; Thiagarajan, P.; Conticello, V. P.; Lynn, D. G. Exploiting Amyloid Fibril Lamination for Nanotube Self-Assembly. *J. Am. Chem. Soc.* **2003**, *125*, 6391–6393.
- (37) Dong, J. J.; Shokes, J. E.; Scott, R. A.; Lynn, D. G. Modulating Amyloid Self-Assembly and Fibril Morphology with Zn(II). *J. Am. Chem. Soc.* **2006**, *128*, 3540–3542.
- (38) Morris, A. M.; Watzky, M. A.; Agar, J. N.; Finke, R. G. Fitting Neurological Protein Aggregation Kinetic Data via a 2-step, Minimal/“Ockham’s Razor” Model: The Finke-Watzky Mechanism of Nucleation Followed by Autocatalytic Surface Growth. *Biochemistry* **2008**, *47*, 2413–2427.
- (39) Morris, A. M.; Watzky, M. A.; Finke, R. G. Protein Aggregation Kinetics, Mechanism, and Curve-Fitting: A Review of the Literature. *Biochim. Biophys. Acta, Proteins Proteomics* **2009**, *1794*, 375–397.
- (40) Watzky, M. A.; Finke, R. G. Transition Metal Nanocluster Formation Kinetic and Mechanistic Studies. A New Mechanism when Hydrogen is the Reductant: Slow, Continuous Nucleation and Fast Autocatalytic Surface Growth. *J. Am. Chem. Soc.* **1997**, *119*, 10382–10400.
- (41) Watzky, M. A.; Morris, A. M.; Ross, E. D.; Finke, R. G. Fitting Yeast and Mammalian Prion Aggregation Kinetic Data with the Finke-Watzky Two-Step Model of Nucleation and Autocatalytic Growth. *Biochemistry* **2008**, *47*, 10790–10800.
- (42) Gillam, J. E.; MacPhee, C. E. Modelling Amyloid Fibril Formation Kinetics: Mechanisms of Nucleation and Growth. *J. Phys.: Condens. Matter* **2013**, *25*, 373101.
- (43) Sievers, S. A.; Karanicolas, J.; Chang, H. W.; Zhao, A.; Jiang, L.; Zirafi, O.; Stevens, J. T.; Munch, J.; Baker, D.; Eisenberg, D. Structure-Based Design of Non-Natural Amino-Acid Inhibitors of Amyloid Fibril Formation. *Nature* **2011**, *475*, 96–100.
- (44) Yoshimura, Y.; Lin, Y.; Yagi, H.; Lee, Y.-H.; Kitayama, H.; Sakurai, K.; So, M.; Ogi, H.; Naiki, H.; Goto, Y. Distinguishing Crystal-Like Amyloid Fibrils and Glass-Like Amorphous Aggregates from their Kinetics of Formation. *Proc. Natl. Acad. Sci. U. S. A.* **2012**, *109*, 14446–14451.
- (45) Hamley, I. W. The Amyloid Beta Peptide: A Chemist’s Perspective. Role in Alzheimer’s and Fibrillization. *Chem. Rev.* **2012**, *112*, 5147–5192.
- (46) Morris, K. L.; Zibaee, S.; Chen, L.; Goedert, M.; Sikorski, P.; Serpell, L. C. The Structure of Cross-beta Tapes and Tubes Formed by an Octapeptide, alpha S beta 1. *Angew. Chem., Int. Ed.* **2013**, *52*, 2279–2283.
- (47) Creighton, T. E. *Protein: Structures and Molecular Properties*, 2nd ed.; W.H. Freeman: New York, 1993; p 507.
- (48) Serpell, L. C. Alzheimer’s Amyloid Fibrils: Structure and Assembly. *Biochim. Biophys. Acta, Mol. Basis Dis.* **2000**, *1502*, 16–30.
- (49) Pedersen, J. S. Analysis of Small-Angle Scattering Data from Colloids and Polymer Solutions: Modeling and Least-Squares Fitting. *Adv. Colloid Interface Sci.* **1997**, *70*, 171–210.
- (50) Pabst, G.; Rappolt, M.; Amenitsch, H.; Laggner, P. Structural Information from Multilamellar Liposomes at Full Hydration: Full q-Range Fitting with High Quality X-ray Data. *Phys. Rev. E: Stat. Phys., Plasmas, Fluids, Relat. Interdiscip. Top.* **2000**, *62*, 4000–4009.
- (51) Oliveira, C. L. P.; Gerbelli, B. B.; Silva, E. R. T.; Nallet, F.; Navailles, L.; Oliveira, E. A.; Pedersen, J. S. Gaussian Deconvolution: A Useful Method for a Form-Free Modeling of Scattering Data from Mono- and Multilayered Planar Systems. *J. Appl. Crystallogr.* **2012**, *45*, 1278–1286.
- (52) Nallet, F.; Laversanne, R.; Roux, D. Modeling X-ray or Neutron-Scattering Spectra of Lyotropic Lamellar Phases – Interplay Between Form and Structure Factors. *J. Phys. II* **1993**, *3*, 487–502.
- (53) Maity, S.; Nir, S.; Zada, T.; Reches, M. Self-Assembly of a Tripeptide into a Functional Coating that Resists Fouling. *Chem. Commun.* **2014**, *50*, 11154–11157.
- (54) Lampin, M.; Warocquier-Clérout, R.; Legris, C.; Degrange, M.; Sigot-Luizard, M. F. Correlation Between Substratum Roughness and Wettability, Cell Adhesion, and Cell Migration. *J. Biomed. Mater. Res.* **1997**, *36*, 99–108.
- (55) Chung, T.-W.; Liu, D.-Z.; Wang, S.-Y.; Wang, S.-S. Enhancement of the Growth of Human Endothelial Cells by Surface Roughness at Nanometer Scale. *Biomaterials* **2003**, *24*, 4655–4661.
- (56) Washburn, N. R.; Yamada, K. M.; Simon, C. G.; Kennedy, S. B.; Amis, E. J. High-Throughput Investigation of Osteoblast Response to Polymer Crystallinity: Influence of Nanometer-Scale Roughness on Proliferation. *Biomaterials* **2004**, *25*, 1215–1224.